Title

The smectic ZA phase: Antiferroelectric smectic order as a prelude to the ferroelectric nematic

Journal

Proceedings of the National Academy of Sciences of the United States of America, 120(8)

ISSN

0027-8424

Authors

Chen, Xi

Martinez, Vikina

Korblova, Eva

et al.

Publication Date

2023-02-21

DOI

10.1073/pnas.2217150120

Peer reviewed

PNAS RESEARCH ARTICLE | PHYSICS

The smectic Z_A phase: Antiferroelectric smectic order as a prelude to the ferroelectric nematic

Xi Chen[a], Vikina Martinez[a], Eva Korblova[b], Guillaume Freychet[c], Mikhail Zhernenkov[c], Matthew A. Glaser[a], Cheng Wang[d], Chenhui Zhu[d], Leo Radzihovsky[a], Joseph E. Maclennan[a], David M. Walba[b], and Noel A. Clark[a,1]

Contributed by Noel A. Clark; received October 10, 2022; accepted December 19, 2022; reviewed by Oleg D. Lavrentovich and Pawel Pieranski

We have structurally characterized the liquid crystal (LC) phase that can appear as an intermediate state when a dielectric nematic, having polar disorder of its molecular dipoles, transitions to the almost perfectly polar-ordered ferroelectric nematic. This intermediate phase, which fills a 100-y-old void in the taxonomy of smectic LCs and which we term the "smectic Z_A," is antiferroelectric, with the nematic director and polarization oriented parallel to smectic layer planes, and the polarization alternating in sign from layer to layer with a 180 Å period. A Landau free energy, originally derived from the Ising model of ferromagnetic ordering of spins in the presence of dipole–dipole interactions, and applied to model incommensurate antiferroelectricity in crystals, describes the key features of the nematic–SmZ_A–ferroelectric nematic phase sequence.

liquid crystal | smectic | antiferroelectric | ferroelectric nematic

Significance

A persistent theme that has emerged from the century-long experimental and theoretical study of ferroelectric crystals and liquid crystals is that ferroelectricity and antiferroelectricity go hand-in-hand, such that if one is found, the other will also be in the same or closely related families of materials. At the root of this behavior is the frustration inherent in steric and electrostatic dipolar interactions, exemplified by the latter, for which dipole pairs arranged end-to-end prefer to be parallel, while dipole side-by-side pairs prefer to be antiparallel. Here, we show that the unexpected recent discovery of the ferroelectric nematic phase and its nearly perfect ferroelectric polar order, is a pathway to antiferroelectricity in fluids, realized in a lamellar smectic array of fluid sheets of alternating polarity.

Proper ferroelectricity in liquids was predicted in the 1910s by P. Debye (1) and M. Born (2), who applied the Langevin–Weiss model of ferromagnetism to propose a liquid-state phase change in which the ordering transition is a spontaneous polar orientation of molecular electric dipoles. A century later, in 2017, two groups independently reported novel nematic phases in the polar molecules of Fig. 1*A*, the "splay nematic" in the molecule RM734 (3–5) and a "ferroelectric-like nematic" phase in the molecule DIO (6). These nematic phases were subsequently demonstrated to be ferroelectric in RM734 (7) and in DIO (8, 9), and a study of their binary mixtures (Fig. 1*B*) showed that these are the same phase, termed N_F here, a uniaxially symmetric, spatially homogeneous, ferroelectric nematic liquid having >90% polar ordering of its longitudinal molecular dipoles (7, 9) (Fig. 1*D*). These mixtures also exhibit, at higher temperatures, a nonpolar, paraelectric nematic (N) phase (Fig. 1*C*). The separate molecular families which RM734 and DIO represent are based on distinctly different molecular structural themes. In the course of the remarkable developments around nematic ferroelectricity, homologous molecules with a variety of substitutions around these themes have been studied, and many of these have also been found to exhibit the N_F phase (8, 10).

The initial study of DIO reported the "M2" phase, a second, unidentified liquid crystal (LC) phase in a ΔT = 15 °C temperature range between the N and N_F phases (Fig. 1*B*) (6). Here, we report that this phase exhibits an equilibrium, sinusoidal electron-density modulation of 8.8-nm periodicity. The M2 is, remarkably, a density-modulated, antiferroelectric phase, exhibiting lamellar (LAM) order with ~17.5-nm periodicity, comprising pairs of 8.8-nm-thick layers of opposite ferroelectric polarization (Fig. 1*D*), related by a reflection plane normal to the director. As in other layered LC phases, these two-dimensional (2D) layers tile three-dimensional (3D) space with fluid spatial periodicity, a structure that largely controls the optic and electrooptic (EO) behavior of bulk samples.

In one of the stunning achievements of condensed matter physics, Georges Friedel combined his optical microscopic observation of elliptical and hyperbolic focal conic defect lines in LCs with knowledge of the Dupin cyclides (complex, equally spaced, 3D-curved surfaces that envelop certain single-parameter families of spheres) to infer the existence of the fluid molecular layer ordering of smectic LCs, without the benefit of X-ray scattering (11). He termed such phases "smectic," following the Greek, as similar structures were found in concentrated solutions of neat soaps (12). Friedel's samples also exhibited what he termed "homeotropy," where the preferred orientation in the smectic of its uniaxial optic axis, the local average long molecular axis, given by the director $\boldsymbol{n}$, is normal to the inferred planes. In time, as understanding of the polymorphism of LCs advanced, it became necessary to subdivide the class of smectic-like phases by structure, and Friedel's specific smectic geometry, the one having $\theta = 0°$, where θ is the angle between the layer normal $\boldsymbol{z}$ and optic axis $\boldsymbol{n}$, was appropriately named the "smectic A" (13). Here, following a path of textural analysis inspired by Friedel, and aided by synchrotron-based small and wide

Author contributions: X.C., V.M., G.F., M.Z., M.A.G., C.W., C.Z., L.R., and N.A.C. designed research; X.C., V.M., E.K., G.F., M.Z., M.A.G., C.W., C.Z., L.R., J.E.M., D.M.W., and N.A.C. performed research; E.K. contributed new reagents/analytic tools; X.C., V.M., M.A.G., L.R., and N.A.C. analyzed data; and X.C., J.E.M., D.M.W., and N.A.C. wrote the paper.

Reviewers: O.D.L., Kent State University; and P.P., Universite Paris-Saclay.

Competing interest statement. The authors have stock ownership to disclose, N.A.C., M.A.G., J.E.M., D.M.W. have partial ownership of Polaris Electro-Optics, the authors have patent filings to disclose, patent filing through University of Colorado Venture Partners, the authors have research support to disclose, research support from Polaris Electro-Optics.

[1]To whom correspondence may be addressed. Email: noel.clark@colorado.edu.

This article contains supporting information online at https://www.pnas.org/lookup/suppl/doi:10.1073/pnas.2217150120/-/DCSupplemental.

Published February 15, 2023.

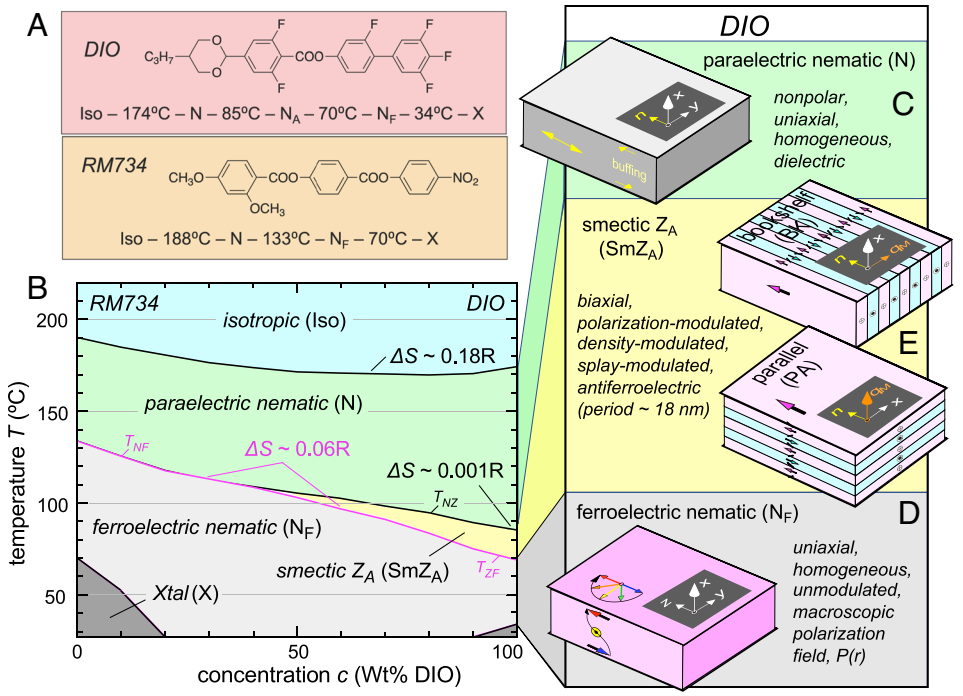

Fig. 1. (*A*) Representative members DIO [(2,3',4',5'-tetrafluoro-[1,1'-biphenyl]-4-yl 2,6-difluoro-4-(5-propyl-1,3-dioxane-2-yl) benzoate] and RM734 [4-[(4-nitrophenoxy) carbonyl]phenyl2,4-dimethoxybenzoate] of nitro- and fluoro-based molecular families of molecules that exhibit the ferroelectric nematic phase. This behavior is attributable in part to their rod-like molecular shape, large longitudinal dipole moment, and a common tendency for head-to-tail molecular association. (*B*) Phase diagram of DIO and RM734 and their binary mixtures exhibiting: (*C*) Paraelectric nematic (N) phase, in which the molecular long axes are aligned in a common direction but with no net polarity, making a nonpolar phase with a large dielectric response. (*D*) Ferroelectric nematic (N_F) phase, in which the polar orientation of dipoles is unidirectional and long-ranged, with a large polar order parameter (~0.9). The N_F phase is uniaxial and spatially homogeneous, with a macroscopic polarization/director field $P(r)$, shown here for antiparallel polar orienting surface alignment layers on the plates (9). The phase diagram shows that the transition temperature into the N_F depends nearly linearly on concentration c, indicating that these molecules exhibit near ideal mixing behavior of the transition into the ferroelectric nematic (N_F) phase. This transition is weakly first-order, with entropy $\Delta S \approx 0.06R$. (*E*) Intermediate phase observed in neat DIO and in DIO-rich mixtures. Originally called the M2 (6), we find this phase to be electron density-modulated into ~9-nm thick, polar layers, in which the director and polarization are parallel to the layer plane and alternate in direction from layer to layer, as sketched. We have termed this lamellar, antiferroelectric phase the smectic Z_A (SmZ_A). The SmZ_A can be prepared with the layers either normal to the plates (bookshelf geometry) or parallel to the plates, or with the chevron texture shown in Figs. 2 and and *SI Appendix* Figs. 6-8.

angle x-ray scattering (SAXS & WAXS), we report a fluid, layered smectic phase with θ = 90°, the structural antipode to Friedel's smectic A, which we classify as the "smectic Z" (14).

Results

X-Ray Scattering. DIO was synthesized using standard synthetic schemes (*SI Appendix*, Fig. S1). SAXS (Fig. 2) and WAXS images (*SI Appendix*, Figs. S2 and S3), obtained upon cooling DIO from the Iso phase with q_z along the magnetically aligned nematic director, show the previously observed (3, 6), intense, diffuse scattering features at $q_z \sim 0.25$ Å^{-1} and $q_y \sim 1.4$ Å^{-1} from end-to-end and side-by-side molecular positional pair correlations, respectively. In the N phase, at small q there is only low-intensity scattering that varies smoothly with q_z. However, upon cooling to the M2 phase, a pair of diffraction spots appear on this background, visible between $T \approx 83$ °C and $T \approx 68$ °C and with the integrated peak intensity a maximum at $T \sim 76$ °C. Scans of intensity through these peaks are shown in Fig. 2*D* and *SI Appendix*, Figs. S4 and S5. Simultaneously observed is a continuous reorientation, without change of shape, of the entire WAXS/SAXS scattering pattern, through an angle $\delta(T)$, starting at $T \approx 83$ °C and reaching $\delta = 12° \pm 1°$ at $T = 75°$, as seen in Fig. 2*B*. The diffraction peaks at T = 75 °C are at wavevector $q_M = 0.071$Å^{-1} (Fig. 2*D*), indicating an electron-density modulation of wavelength $w_M = 8.8$ nm, with $\boldsymbol{q}_M$ along $\boldsymbol{y}$, normal to the nematic director, the local mean molecular long-axis orientation, $\boldsymbol{n}$, along z. The WAXS peak at $q_y \sim 1.4$ Å^{-1} corresponds to a side-by-side molecular spacing in DIO of ~0.42 nm in the direction of the modulation, so the period of this modulation is supermolecular, ~20 molecules wide. The growth of such a periodic structure in a uniaxial, field-aligned nematic should give powder scattering in the (q_x,q_y) plane normal to $\boldsymbol{n}$. That only a single pair of diffraction spots appear indicates that there is only a single diffraction ring in this plane intersecting the Ewald sphere (approximately the (x,z) plane), indicating that this ordering could be either 1D lamellar smectic-like, or 2D hexagonal columnar. The textural studies and electro-optic experiments presented below show definitively that this is a lamellar phase. Macroscopically, this phase is a fluid, as confirmed by its diffuse scattering features in the WAXS, which differ very little from those of the fluid nematic phase (*SI Appendix*, Fig. S2). This observed phase sequence is consistent with that of earlier reported DIO studies (6, 9, 15), indicating that it is the trans form of DIO that is being studied [*SI Appendix*, (15)].

As indicated above, the diffraction pattern rotates on cooling, with the lateral diffraction spots remaining in the equatorial plane of the SAXS/WAXS patterns. This implies that the entire sample volume probed by the beam (a 1-mm × 2-μm × 20-μm cylinder), the director $\boldsymbol{n}$, and the layering wavevector $\boldsymbol{q}_M$, have all uniformly reoriented together through $\delta(T)$, a rotation of $\boldsymbol{n}$ away from the orientation preferred by the magnetic field. This kind of temperature-dependent director/layer reorientation accompanying layer formation upon cooling of smectic LCs has been observed in magnetically aligned (16) and surface-aligned (17) samples undergoing nematic to smectic A (SmA) to smectic C (SmC) (18–20) or N to SmC phase transitions upon cooling (21), in

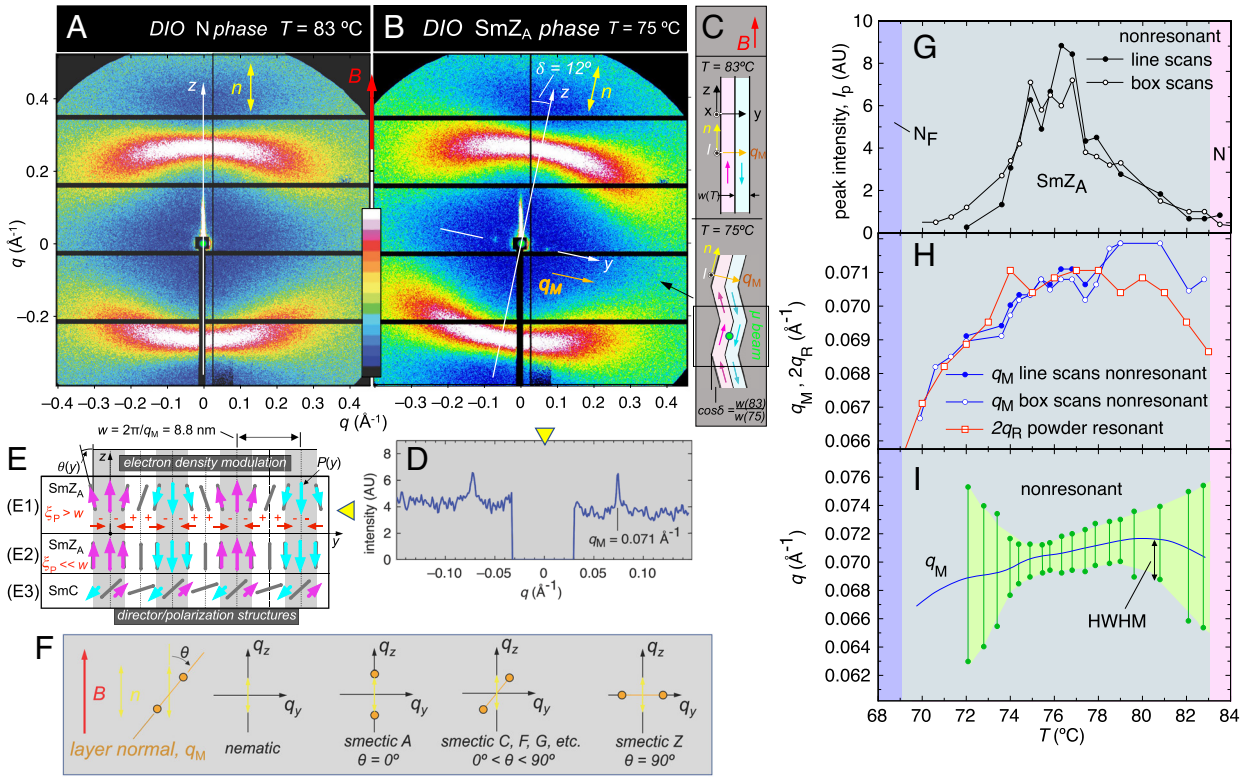

Fig. 2. SAXS scattering from the N and SmZ_A phases of DIO. These diffractograms are from a sample in a 1 mm-diameter capillaries in which the director, *n*, is aligned along the magnetic field *B* (red), studied on the SMI microbeam line at NSLS II. (*A* and *B*) Non-resonant diffractograms obtained on cooling show a diffuse scattering arc at $q_z = 0.25 Å^{-1}$ from head-to-tail stacking of the molecules in the N and SmZ_A phases. In the SmZ_A phase, equatorial Bragg spots appear, indicating the presence of an electron density wave of $w_M = 8.8$-nm periodicity, with wavevector $\boldsymbol{q}_M$ normal to $\boldsymbol{n}$. These peaks disappear upon transitioning to the N_F phase (*G*, *SI Appendix*, Figs. S4 and S5). (*C*) The scattering pattern rotates from (*A*) to (*B*) because of layer reorientations caused by a small reduction in layer thickness upon cooling in the SmZ_A phase (see text). (*D*) Line scan through the non-resonant scattering peaks. The central part of the beam is blocked by the beam stop. (*E*) Since the sample is a powder in orientation about the *B* field, the observed scattering pattern could be indicative of either lamellar or hexagonal columnar positional ordering. Since non-resonant scattering is sensitive only to electron density, the layers (of thickness w_M) of opposite polarization scatter identically. Layer boundaries (white stripes) have different electron density than the layer centers (gray stripes), making w_M the period observed in nonresonant scattering. However, as shown in (*H*) and *SI Appendix*, Fig. S5, carbon-edge resonant scattering exhibits the half-order peak at $q_R = q_M/2$, showing conclusively that the SmZ_A is lamellar and bilayer with period $2w_M$. The DTOM experiments show that it is lamellar and antiferroelectric, with layers of alternating polarization $P(y)$, sketched in (*E1*) for low polarization ($\xi_P > w$), and in (*E2*) for high polarization ($\xi_P << w$), the case relevant to the SmZ_A (see text). The tilt modulation $\theta(y)$ is suppressed at large *P* by the self-electric field due to the polarization charge, $\rho = -\nabla \cdot P$, indicated in red. Other smectic structures (e.g., the SmC, sketched in *E3*) have spontaneous antiferroelectric polarization in the tilt plane as well as splay modulation *SI Appendix*, Section 8), but in different geometries. (*F*) X-ray scattering peaks from various smectics with the director aligned by the magnetic field *B*. (*G–I*) Dependence on *T* of the Bragg peak parameters from data as in *SI Appendix*, Figs. S4 and S5 [non-resonant peak intensity (I_p), non-resonant peak position ($\boldsymbol{q}_M = 2\pi/w_M$), resonant peak position ($q_R = 2\pi/2w_M$), and non-resonant half-width at half-maximum ($HWHM_M$)]. (*H*) Layers of opposite *P* have different carbon K-edge resonant scattering cross-sections, and therefore Bragg scatter at the full antiferroelectric period $2w_M$. (*I*) The $HWHM_M$ values of the mid-range peaks ($T \sim 75$ °C) are SAXS-resolution limited.

the context of the study of surface-stabilized ferroelectric LCs (22). This behavior is understood to be a result of fluid smectic layers contracting everywhere upon cooling, in the SmC case due to an increasing tilt of the molecular long axes away from the smectic layer normal with decreasing temperature. The result of layers of thickness $w_M(T_1) = 2\pi/q_M(T_1)$ growing into a bulk sample at temperature T_1 with an aligned director and then homogeneously shrinking in thickness upon cooling to T_2 is sketched in Fig. 2*B*. A local reorientation of the layers through the angle $\delta(T) = \cos^{-1}[w_M(T_2)/w_M(T_1)]$, under conditions of low compressive stress of the layering, preserves the original pitch, $w_M(T_1)$ of the layering as it was initially formed. In a large (1-mm diameter) X-ray capillary, the pattern of such reorientation is complex, and different on each cooling run. On a larger scale, defects, such as parabolic focal conics (23) or the planar breaks of a chevron structure sketched in Fig. 2*C*, mediate changes in the sign of $\delta(T)$. In the experiment shown in Fig. 2, the scattering volume was fortuitously filled with a single such reorienting domain. In thin cells with alignment layers, layer shrinkage is typically accommodated by the chevron layer structure and its characteristic defects, discussed below.

These observations and, in particular, the simple appearance of the scattering pattern in Fig. 2*B*, make it clear that the M2 is a form of fluid, lamellar phase with layer planes normal to a density modulation wavevector $\boldsymbol{q}_M$, which is, in turn, normal to the mean molecular long-axis $\boldsymbol{n}$, constraining $\boldsymbol{n}$ to be parallel to the (x,z) plane of the layers. Such a structure is orthorhombic biaxial, with a principal symmetry/optic axis triad ($\boldsymbol{l}$, $\boldsymbol{q}_M$, $\boldsymbol{n}$), where $\boldsymbol{l}$ is the auxiliary unit vector normal to the $\boldsymbol{q}_M$, $\boldsymbol{n}$ plane. Related biaxial lamellar phases have been achieved only in amphiphilic systems, such as the "LAM_N" phase in bola-amphiphiles (24), and the hybrid DNA/cationic liposome lamellar phases (25), which employ strong nanophase segregation to isolate anisotropic 2D nematic-like molecular monolayers within a lamellar phase. We will show that in the M2 phase each layer is structurally and electrically polar, with alternating polarity from layer to layer, an antiferroelectric condition shared by some biaxial phases of bent-core molecules (26).

Finding similar behavior in a molecule as simple as DIO is truly remarkable, so we classify this phase to be among the thermotropic smectics of rod-shaped mesogens, as sketched in Fig. 2*F*, naming it the smectic Z, such that the smectic A, the phase having $\boldsymbol{q}_M$

parallel to $\boldsymbol{n}$ (θ = 0°), and the smectic Z, the phase having $\boldsymbol{q}_M$ normal to $\boldsymbol{n}$ (θ = 90°) represent the lower and upper limits of tilt angles, θ. We may also consider that the M2 could be classified as a kind of nematic, in analogy with the twist-bend nematic (N_{TB}) phase. The N_{TB} phase is characterized by a spontaneous, heliconical precession of the nematic director, a periodic modulation that is helically (C_∞) glide symmetric and therefore has no accompanying electron density variation or nonresonant X-ray scattering: different positions along the helix are relatively rotated but otherwise physically equivalent, making the N_{TB} a kind of nematic, with a modulation that requires the use of resonant scattering in order to be observable with X-rays. However, in the case of a finite-amplitude, periodic modulation of the director orientation involving splay and/or bend, as we report below and sketch in Fig. 2*E*, for example, there is no equivalent translational symmetry, as planes with maximum and zero director distortion, or with a particular polarization magnitude, are inequivalent and therefore have different electron density. Such structures are therefore smectic. In the literature, there are many proposals for, and examples of, polar-modulated nematic director fields based on structures that have director splay and bend (27), including the splay nematic model proposed for the N_F phase of RM734 (4, 5), but all such model systems will have corresponding modulation in density. Those with 1D modulation are smectic, as is directly demonstrated here by the non-resonant SAXS in Fig. 2 and *SI Appendix*, Figs. S4 and S5, exhibiting the ~9-nm periodic density modulation. Additionally, resonant SAXS results in Fig. 2 and *SI Appendix*, Fig. S6 show that the SmZ_A is antiferroelectric, with adjacent 9-nm layers exhibiting opposite polarization along $\boldsymbol{n}$, and delineated by planes of zero average polarization parallel to $\boldsymbol{n}$.

The observation of a single pair of diffraction spots (no harmonics) for both the nonresonant (Fig. 2 and *SI Appendix*, Fig. S4) and resonant (*SI Appendix*, Fig. S5) scattering suggests that the density modulation of the layering at $\boldsymbol{q}_M$, and the polarization modulation at $\boldsymbol{q}_M/2$ may be nearly sinusoidal. However, this notion should be considered with caution, as the scattering peaks appear with substantial background noise, so that lower intensity harmonics may be present but not visible in these experiments.

Optical Textures and EOs. The X-ray scattering suggests that the SmZ phase should be optically biaxial, with the principal axes (x,y,z) of its optical dielectric tensor ($\boldsymbol{x} \parallel \boldsymbol{l}$, $\boldsymbol{y} \parallel \boldsymbol{q}_M$, $\boldsymbol{z} \parallel \boldsymbol{n}$, as in Figs. 3 and 4). Textures visualized using depolarized transmission optical microscopy (DTOM) in Fig. 3 show the planar alignment achieved on cooling a d = 3.5-μm antiparallel-rubbed cell with a 3° angle between the buffing direction and the in-plane electrode edges. In absence of applied field, the N–SmZ_A transition is difficult to observe optically, although there is a small increase in birefringence $\delta\Delta n_{yz} \approx 0.008$ across the phase transition (compare Fig. 3 *A*–*D*). Excellent extinction is obtained for optical polarization along the buffing direction in both the N and SmZ_A phases (compare Fig. 3 *B*–*E*). The subsequent transition to the N_F, on the other hand, is quite dramatic, with no extinction observed for any sample orientation in the twisted N_F state (28) (Fig. 3 *G* and *H*). Fig. 3 *C*–*F* show the same ~1.5 mm long section of this cell as in Fig. 3*B* but with a very slowly time-varying, effectively DC, field applied, at 30 V/mm. In the N phase (Fig. 3*B*), this field generates a twist Freedericksz transition, shown for E = 30 V/mm in the center of the electrode gap, whereas in the slowly growing-in SmZ_A phase (Fig. 3*C*), this transition is suppressed.

The in-plane electric field can induce a dielectric twist Freedericksz transition in the N phase at a threshold field as small as ~10 V/mm. The 3° bias of the buffing direction means that the director $\boldsymbol{n}$ initially makes an angle of 87° with the field $\boldsymbol{E}$, so that the initial dielectric field-induced twist reorientation of $\boldsymbol{n}$ is everywhere in the same azimuthal direction (the direction that reduces the angle between the director and the applied field). The initially uniform cell shows good extinction at E = 0, but the applied electric field causes a twist distortion of the director field that results in transmission of light that increases with field strength, as illustrated by the white-light DTOM intensity profiles plotted in Fig. 3*I*. Under the same field conditions in the SmZ_A phase, however, there is no discernable optical response, as is evident from Fig. 3*J*, indicating that the director reorientation is suppressed in the SmZ_A phase, either by elimination of nematic dielectric torques, or by structure that strongly limits reorientation. The former possibility can be ruled out because the nematic dielectric torques are proportional only to the dielectric anisotropy $\Delta\varepsilon$, which does not change substantially at the N–SmZ transition in DIO (4, 5). However, the latter phenomenon is quite familiar in smectic A phases. For example, the splay-bend Freedericksz reorientation observed when an in-plane electric field is applied to a homeotropically oriented cell of a nematic with $\Delta\varepsilon > 0$ is eliminated at the N–SmA phase transition by the appearance of a local potential energy that keeps $\boldsymbol{n}$ along the smectic layer normal (29, 30). The restoring torque maintaining $\boldsymbol{n}$ normal to the plates in the SmA phase is not that of Frank elasticity over a micron-scale cell gap, d, but rather that of a local potential energy well [Friedel homeotropy (11)] that is typically stronger than the Frank elasticity by a large factor ~$(d/l)^2$, where l is the nanometer-scale smectic layer thickness. This, combined with the condition that the smectic layering is essentially immovable at typical nematic Freedericksz threshold fields, suppresses molecular reorientation except under conditions of catastrophic layer reorganization at very high fields. In the SmZ phase, similar considerations explain why rotation of $\boldsymbol{n}$ out of the layer plane is suppressed.

The EO response to applied field can provide definitive information on how the SmZ_A layers organize upon cooling from the N phase. With $\boldsymbol{n}$ planar-aligned along the buffing direction, the layers will tend to order spontaneously either parallel to the plates (PA), or in "bookshelf" geometry (BK), as depicted in Fig. 1*E*, with the layers normal to the plates or nearly so. In the parallel geometry, an in-plane field readily induces in-plane reorientation of $\boldsymbol{n}$, with, since $\boldsymbol{E}$ is normal to $\boldsymbol{n}$, dielectric-like linear induced polarization response of the antiferroelectric structure driving twist deformation opposed by Frank elasticity. In the bookshelf geometry, on the other hand, molecular reorientation in the plane of the cell would force molecules out of the plane of the SmZ layers, a locally resisted, high energy deformation (28, 29). Suppression of the twist Freedericksz response in a particular cell therefore indicates that the layer normal $\boldsymbol{y} \parallel \boldsymbol{q}_M$ is essentially parallel to the plates.

Bookshelf and Chevron Layer Structures. Further DTOM observations of the grown-by-cooling SmZ_A cell textures show that the layers typically adopt bookshelf (BK) geometry at the N–SmZ_A transition, with the layers normal to the plates. However, as illustrated in Fig. 2*C*, the layers contract slightly with decreasing temperature, and the layers respond by buckling (Fig. 2*C*), leading to the "chevron" (CH) variant of the lamellar bookshelf geometry (Fig. 4*D* and *SI Appendix*, Figs. S6–S10), in which the layer normal exhibits a step reorientation at the chevron interface (18–21), a planar surface parallel to the plates where the layer tilt δ changes sign. This structure maintains the locations of the contact lines of the layers at the surfaces and the uniform |δ| maintains the bulk layering pitch along $\boldsymbol{y}$ (in the plane of the cell), $p = 2\pi/q_M(T_{NZ})$, that was established on the surfaces and in the bulk at the N-SmZ_A transition.

The chevron structure and the associated zig-zag walls stand on the same footing as Friedel's focal conics as being fundamental

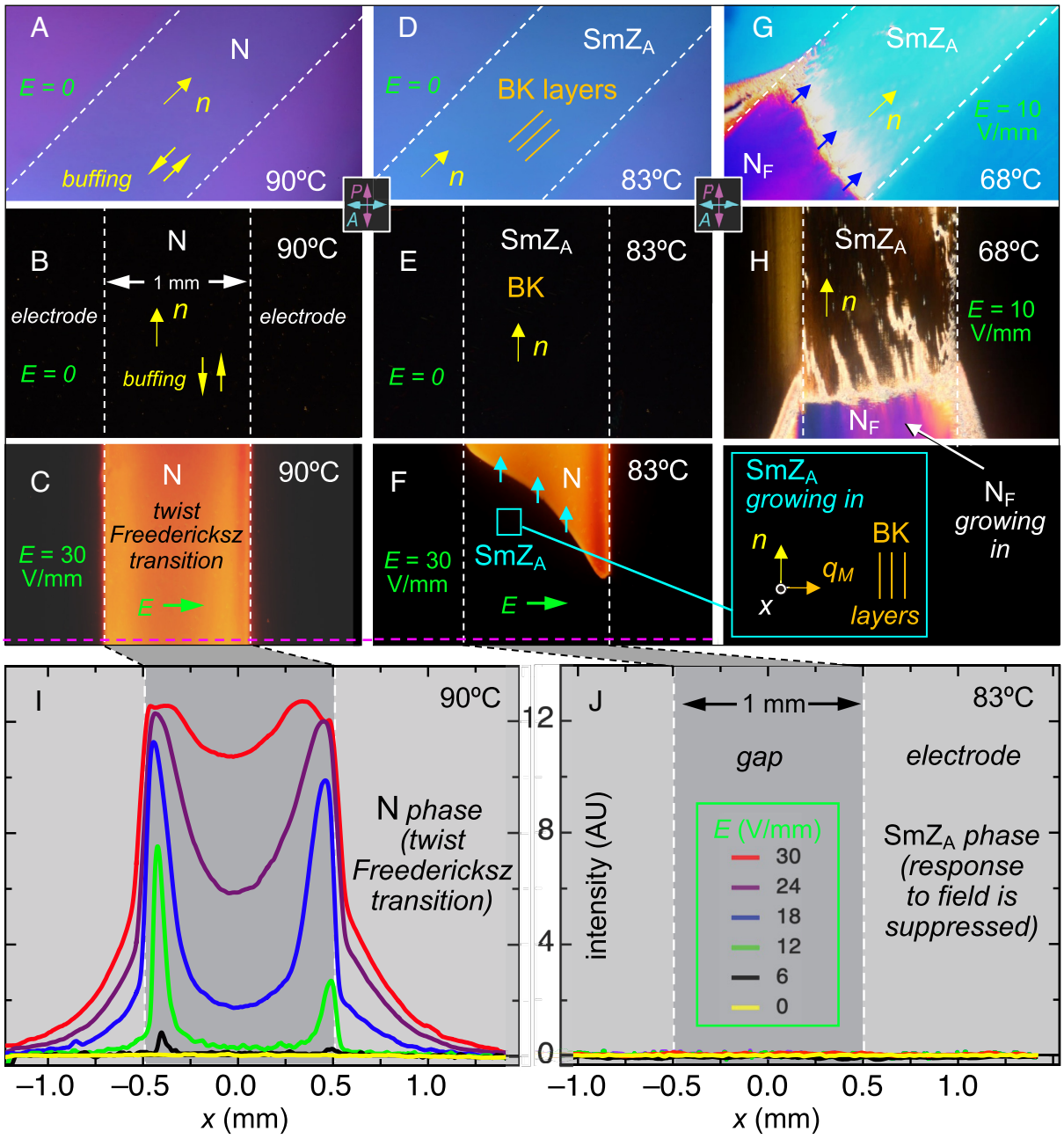

Fig. 3. Textures of DIO in a d = 3.5-μm cell with in-plane electrodes spaced by 1 mm and antiparallel buffing parallel to the electrode edges, cooled at −1 °C/min and viewed in DTOM with polarizer and analyzer as indicated. (*A*–*C*) Planar-aligned nematic monodomain with n parallel to the plates and to the electrode edges, showing (*A*) a birefringence color corresponding to d = 3.5 and Δn = 0.18, (*B*) excellent extinction with n parallel to the polarizer, and (*C*) the transmission due to twist of n during a field-induced twist Freedericksz transition. (*D* and *E*) Bookshelf-aligned (BK) smectic Z_A monodomain formed on cooling. The smectic layers are parallel to n and normal to the cell plates. The birefringence is slightly larger than in the nematic phase and excellent extinction is again obtained with n parallel to the polarizer. (*F*) Optical response of coexisting nematic and SmZ_A phases to an applied 200-Hz square wave field of peak amplitude, E. The nematic region undergoes a twist Freedericksz transition but in the smectic Z_A phase, rotation of the director is suppressed by the layering. (*G* and *H*) N_F phase growing into the SmZ_A upon further cooling. The antiparallel buffing stabilizes a π-twist state in the polarization/director field of the N_F, which does not extinguish between crossed polarizer and analyzer at any cell orientation. (*I* and *J*) Optical intensity scans along the magenta dashed lines across the bottom of the images in (*C* and *F*), probing the electric field-induced in-plane twist Freedericksz reorientation in the N_F phase and showing that there is no observable electro-optic effect in the SmZ_A phase. In this geometry, where the layers have bookshelf (BK) alignment, an in-plane field would tend to rotate the director out of the smectic layer planes, a deformation that is locally resisted by the SmZ_A structure.

layering defects of smectics: focal conics result from step orientational discontinuities along lines, whereas chevrons result from step orientational discontinuities on sheets. Zig-zags are higher energy defects that appear when the requirement in buffed cells to satisfy the constraint of uniform orientation at the surfaces does not permit focal conics. Zig-zag walls have been extensively studied in systems undergoing the N–SmA–SmC (18) and N–SmC (20) transitions, where the layer shrinkage is due to tilt of the molecular long-axis away from the layer normal in the SmC phase. Typical SmC zig-zag wall textures are shown in *SI Appendix*, Figs. S6 and S7–S10. An analogous texture of zig-zag walls obtained on cooling DIO from the N to the SmZ_A phase is shown in Fig. 4. In this case, a small, in-plane square-wave electric field was applied along $\boldsymbol{q}_M$ to alternate the direction of the nascent chevrons as they formed, giving a texture having an array of zig-zag walls.

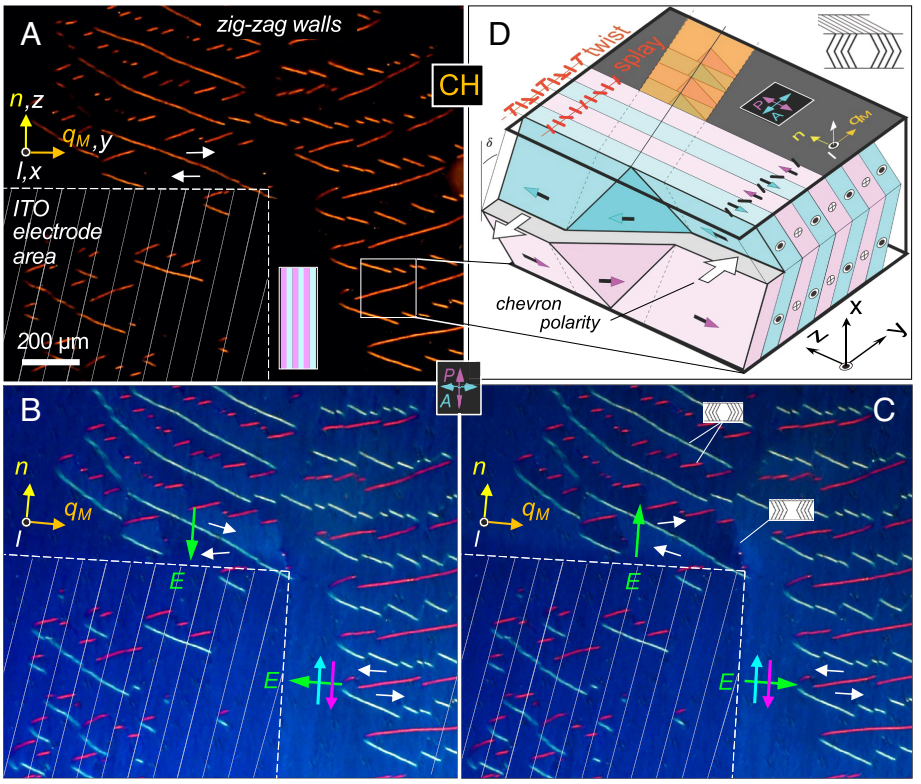

Fig. 4. Zig-zag defects in a SmZ_A cell with chevron layering confirm the lamellar structure of the SmZ_A. Zig-zag walls appear in smectic cells originally with the layers substantially normal to the cell plates (bookshelf geometry) when the layers are caused to shrink in thickness. A common response to accommodate layer shrinkage in thin cells where there is surface pinning is for the layers to tilt, forming the chevron variation (CH) in bookshelf alignment, and zig-zag walls are the layering defects which mediate binary change in the pointing direction of the chevron tip. (*A*–*C*) Zig-zags generated in the SmZ_A phase as it is grown by cooling in a weak electric field (1 Hz square-wave, ~10 V/mm). Zig-zag walls are of two types, sketched in (*C*): "diamond" walls [⟨⟨⟨⟨⟩⟩⟩⟩], detailed in (*D*), where the chevrons point out from the wall center, and which run nearly along $\boldsymbol{q}_M$, i.e., nearly normal to the layers; and "broad" walls [⟩⟩⟩⟩⟨⟨⟨⟨], where the chevrons point in toward the defect wall, which run parallel to the layers and to the director, ***n***. These zig-zag walls are analogous to those found in planar-aligned SmC and SmC* cells (*SI Appendix*, Fig. S7). (*D*) Detailed structure of a diamond wall in which the normal to the diamond-shaped layer elements is rotated to make an angle with the cell normal that is larger than the layer tilt angle, δ, of the chevrons, enabling the wall to space out the chevron tips in opposite directions (21). The orientation and birefringence of the diamonds walls causes them to transmit light when the overall chevron structure is at or near extinction, as in (*A*–*C*). The orientation of the diamond elements can be determined from their extinction angle (SI Appendix, Fig. S8*C*). The broad wall structure is less visible in the SmZ_A than in the SmC cells shown in *SI Appendix*, Fig. S6 because in the SmZ_A the rotations of layer elements in the wall do not result in reorientation of ***n***. The presence of fringing fields near the electrodes [marked with white dashed lines in (*B* and *C*)] enables ***E*** fields to be applied either parallel or and normal to ***n*** in separate regions of the cell. The difference in optical saturation observed in these regions for different signs of field applied parallel to ***n*** (*B* and *C*) reveals that the polarity of the chevron structure generates an interfacial polarization that is indicated by the white arrows: the chevron areas are polar along ***y***, with the white arrows rotating in opposite directions on opposite sides of a zig-zag wall, indicating a polar rotation of the director near the chevron interface when a field $\boldsymbol{E}_z$ is applied. In contrast, with the field along ***y*** there is no polar reorientational response of the director to change of field sign (*B* and *C*), indicating that the AF cancels the net polarization in the bulk (magenta, cyan arrows). The red twist and splay schematics are the possible director modulations considered in calculating the biaxial birefringence $\Delta n_{biax} \equiv n_q - n_l = \Delta n_{PA} - \Delta n_{BK}$ (see text) of the SmZ_A. Measurement shows that $\Delta n_{biax} > 0$, indicating a splay modulation of ***n***.

We probed the polar characteristics of the as-grown chevron domains by applying small, in-plane electric fields both parallel to the layers (along ***n***) and perpendicular to them (along $\boldsymbol{q}_M$), the latter achieved using fringing fields near the upper edge of one of the rectangular electrodes, as shown in Fig. 4 *B* and *C*. As can be seen, the field generated parallel to ***n*** by the upper electrode edge induces a difference in hue between the chevron domains on opposite sides of zig-zag walls, indicating field-induced director rotation that is uniform over the domain, but in opposite directions in domains with opposite chevron direction. This implies a polarization of the chevron domains as indicated by the white arrows in Fig. 4 *B*–*D*, leading to field-induced director reorientation near the chevron interface. Such polarity, arising from the layer structure, is consistent with the directionality of the chevron. On the other hand, where the applied field is normal to ***n*** (at the right electrode edge), there is no observable director reorientation, indicating that as the SmZ_A is grown, it has no net component of polarization parallel to ***n*** (cyan, magenta arrows), evidence for antiferroelectricity (AF).

Observation of AF of the SmZ_A Phase. Increasing the field to ~10X, the Freedericksz threshold in *SI Appendix*, Fig. S9*F* reorients the director toward being normal to the plates. If a field in this range is applied to the sandwich cell filled with zig-zags as in *SI Appendix*, Fig. S9 *B* and *C* or if bookshelf alignment is obtained by cooling from the N phase with a comparable field applied, the chevron layering defects, which rarely disappear on their own, can be forced out, and monodomain bookshelf alignment with the layers uniformly oriented normal to the plates achieved (*SI Appendix*, Fig. S9*E*). These monodomains also exhibit the splay-bend Freedericksz transition at low applied fields (*SI Appendix*, Fig. S9*F*), but at higher fields, they provide key evidence for the antiferroelectric nature of the SmZ_A phase. The I-V characteristics of a $d = 100$ μm, bookshelf indium-tin oxide (ITO)-sandwich cell with a 5 Hz, 50 V/100-μm amplitude triangle wave electric field applied along ***n*** during an N–SmZ_A–N_F cooling scan are shown in Fig. 5*A*. At high temperatures, in the N phase ($T > 84$ °C), the current shows the usual cell capacitance step and an ion bump. In the SmZ_A phase (84 °C > T > 68 °C), new polarization peaks appear at the highest voltages, growing in area and with their peak

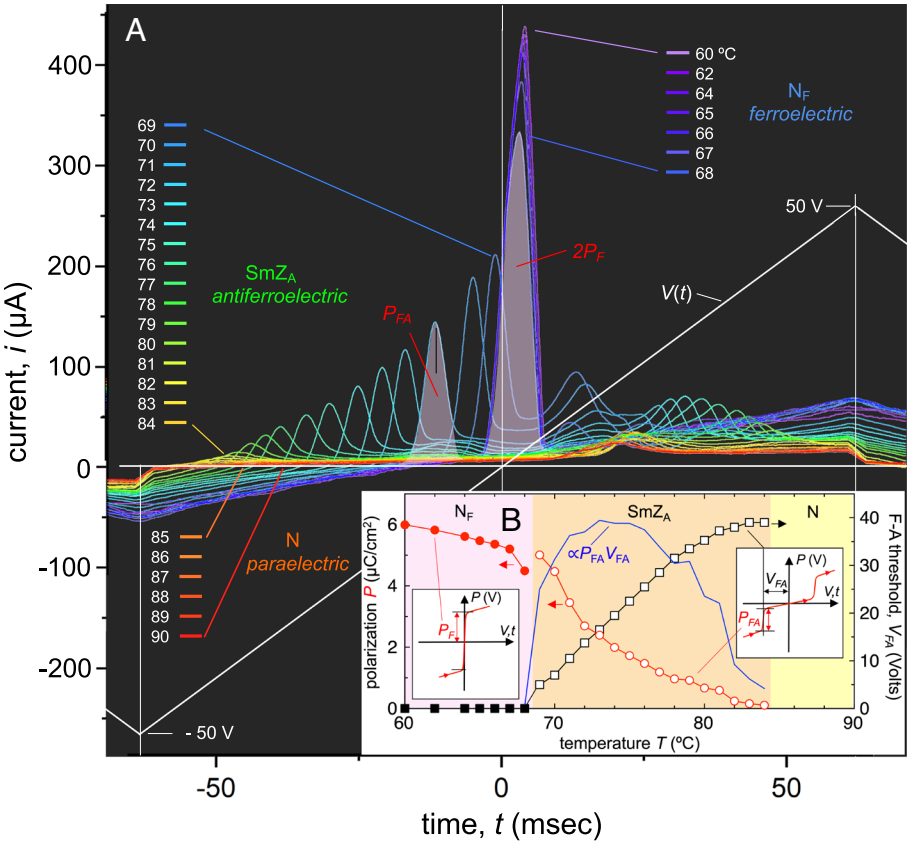

Fig. 5. (*A*) Measured *I*(*t*)-*V*(*t*) characteristics of DIO as a function of temperature, revealing a large field-induced shift in the SmZ_A–N_F phase transition temperature for electric field $E_z = V(t)/100\mu m$, applied along ***n***. The plot shows the current response *I*(*t*) of DIO in a $d = 100$ μm sandwich cell with bare ITO electrodes generating bookshelf layering, to a 5 Hz, 50 V amplitude triangle wave [*V*(*t*), white curve] applied during an N–SmZ_A–N_F cooling scan. In the N phase ($T > 84$ °C), the current shows the expected cell capacitance step and an ion bump. In the SmZ_A phase (84 °C > *T* > 68 °C), new polarization peaks appear at the highest voltages, growing in area, with their peak center voltages V_{FA} becoming smaller on cooling. This is typical antiferroelectric behavior, the peaks marking the transition at finite voltage between the field-induced ferroelectric (F) state and the equilibrium antiferroelectric (*A*) state. (*B*) Polarization values $P_{FA}(T)$ [open circles] and ferroelectric-to-antiferroelectric depolarization voltage $V_{FA}(T)$ [open squares] obtained from the depolarization current response (in the time range $t < 0$), where there is the least interference from ion flow). The corresponding field $E_{FA}(T) = V_{FA}(T)/100\mu m$. The open squares give the first order SmZ_A–N_F phase boundary in the (E_z–*T*) plane, and the open circles the polarization change P_{FA} at this transition. According to the Clausius–Clapyron equation, the transition entropy, Δ*S*, also decreases with increasing E_z along this line, to zero at the maximum E_z. The blue curve is proportional to the product $P_{FA}(T)V_{FA}(T)$, and therefore proportional to the stabilization energy of the antiferroelectric state, which is maximum at $T = 73$ °C. The SmZ_A to N_F transition occurs between T = 69 °C and 68 °C, with the current transforming to a single peak centered around $V = 0$, typical of field-induced, Goldstone-mode reorientation of macroscopic polarization, P_F [red solid circles]. This peak area corresponds to a net polarization comparable to that measured in the N_F phase of RM734 (7).

center voltages V_{FA} moving to lower magnitudes as *T* decreases. This is typical antiferroelectric behavior, the peaks marking the transition at finite voltage between the field induced ferroelectric (F) state at high fields, and the low-field antiferroelectric (A) state. The time integral of this current, $Q = \int i(t)dt$ gives the magnitude of polarization reversal in the antiferroelectic–ferroelectric transition, $P_{FA}(T) = Q(T)/A$, where *A* is the electrode area. Both the polarization $P(T)$ and the transition voltage, $V_{FA}(T)$ are plotted in Fig. 5*B*. The open squares give the first-order SmZ_A–N_F phase boundary $E_{FA}(T) = V_{FA}(T)/100\mu m$ in the (E_z–*T*) plane, and the open circles the polarization change P_{FA} at this transition (*SI Appendix*, Fig. S13). The transition entropy Δ*S* decreases along this line to zero at the maximum E_z, according to the Clausius–Clapyron equation. Also shown is the product $P_{FA}(T) \times V_{FA}(T)$, proportional to the stabilization energy of the antiferroelectric state, which is maximum in the middle of the SmZ_A temperature range. These observations clearly establish that the SmZ_A phase is antiferroelectric. The SmZ_A to N_F transition occurs between 69 °C and 68 °C, with the current transitioning to a single peak near $V = 0$, as seen in Fig. 5*A*, corresponding to the field-induced, Goldstone-mode reorientation of a macroscopic polarization, P_F. The measured polarization in the N_F phase is comparable to values previously obtained for DIO (7). Recently, Brown et al. have reported evidence for "local antiferroelectric" behavior in the M2 phase of DIO (31), and Nacke et al. have observed antiferroelectric polarization behavior in an intermediate phase between N and N_F in a different fluorinated material (32).

Bookshelf to-Parallel Layering Transformation. If a low-frequency (20 mHz) in-plane triangle electric field is applied to the bookshelf SmZ_A cell and its amplitude increased above about 80 V/mm, ferroelectrohydrodynamic flow is generated (7), which disrupts the SmZ_A layering. The field-induced polarization tends to orient along the field direction, and in doing so restructures the layers in some areas, switching them from the bookshelf (BK) orientation to be parallel to the plates (PA), a process shown in *SI Appendix*, Figs. S11 and S15. When the field is reduced, the PA areas anneal into highly ordered monodomains filling the thickness of the cell with the SmZ_A layers parallel to the plates as sketched for the PA geometry in Fig. 1*D*. The director ***n*** remains along the buffing direction, so that the layers have effectively been rotated by 90° about ***n*** from the original bookshelf geometry. Near the N–SmZ_A transition, a typical cell treated in this way can simultaneously exhibit N, SmZ_A bookshelf, and SmZ_A parallel domains, as seen in *SI Appendix*, Figs. S11 and S15 *B*–*D*.

As in the N phase, the SmZ_A parallel domains respond to in-plane applied fields by exhibiting a field-induced azimuthal reorientation of $\boldsymbol{n}(x)$ about $\boldsymbol{x}$, the normal to the cell plates. EO observations discussed in *SI Appendix*, sectionS8 with in-plane fields normal to $\boldsymbol{n}$, are summarized in *SI Appendix*, Fig. S15 showing this orientational response to be a strictly dielectric-driven, twist Freedericksz transition as in the N phase. This confirms that the bulk polarization density along $\boldsymbol{n}$ is zero, i.e., that, at fields well below those required to induce the AF to F transition, the field-free SmZ_A phase has zero net ferroelectric polarization, and its linear response at small field is purely dielectric.

Biaxiality and the Modulation Structure of the SmZ_A Phase. The simultaneous presence of bookshelf and parallel domains in planar aligned cells enables a measurement of features of the optical biaxiality of the SmZ_A phase, as detailed in *SI Appendix*, section S9 and Fig. S16.

Discussion: Modeling The N–SmZ_A–N_F Phase Diagram

A persistent theme that has emerged from the century-long experimental and theoretical study of ferroelectric materials, both crystals and LCs, is that ferroelectricity (F) and AF go hand-in-hand, such that if one is found, the other will be in related materials, and even phase coexistence of the two in equilibrium in a given material is a common phenomenon. At the root of this behavior is the inherent frustration of dipole–dipole steric and electrostatic interactions, e.g., for the latter, dipole pairs arranged head-to-tail prefer relative parallel orientation, whereas side-by-side dipole pairs prefer relative antiparallel orientation. This frustration is almost a recipe for generating modulated AF phases of the SmZ_A type, having ferroelectric stripes of uniform $\boldsymbol{P}$ in the end-to-end direction, and antiferroelectric ordering of adjacent stripes in the side-by-side direction. Thus, in trying to understand the first AF phase of the ferroelectric nematic realm, we are moved to explore the basic physics of this F/AF relationship in pursuit of theoretical modeling of the SmZ_A.

Our observations identify the SmZ_A to be a kind of spontaneously modulated phase, of which there are many examples in soft materials (33, 34), LCs (26, 33–36), and ferroelectric (or ferromagnetic) solids (37–41). Such modulated phases have been explored by theory and simulation of equilibrium states in systems of molecular-scale (e.g., spin) variables, as well as with coarse-grained and Landau theoretical modeling of their mesoscopic averages as fields. The observation of both the N–N_F and N–SmZ_A–N_F phase sequences in the RM734/DIO binary phase diagram of Fig. 1 presents a new paraelectric–antiferroelectric–ferroelectric experimental landscape, one that ideally is viewed theoretically as a feature of some common ordering process. Among modulated states found in ferroelectric or ferromagnetic materials are the antipolar-ordered stripe phases, which appear in a wide variety of theoretical and experimental systems exhibiting the above-mentioned frustration arising from competing ferroelectric short- and antiferroelectric-long-range (power law) interactions in 2D and 3D (35, 36, 40–44). These modulated phases exhibit various periodic patterns of alternating polarity (44), and at finite temperature they are observed to order in patterns that can be either multi-unit-cellular or incommensurate, the latter having periods that are not rational fractions of the unit cell period of an underlying crystal lattice (42, 45).

An important theoretical approach to understanding the physics of such modulated systems are models where macroscopic polarization $P_z(\boldsymbol{r}) = n\langle p_{zi}\rangle$ is calculated as a local average of molecular-scale dipoles p_{zi} of number density n, interacting with a Ising Hamiltonian,

$H = \sum \left(J_{ij} + D_{ij}\right) p_{zi} p_{zj}$, typically employing variables of binary sign, p_{zj}, having local ferro-like interactions J_{ij}, and long-range dipole–dipole interactions D_{ij} (40, 41, 44–47). The frustration introduced by the anisotropy of the dipolar interaction, can stabilize transverse periodic modulation of the macroscopic polarization $P_z(y)$, while at the same time suppressing spatial variations $P_z(z)$ that separate opposite signs of polarization space charge $\rho_P = \nabla\cdot\boldsymbol{P}(\boldsymbol{r})$ and increase Coulomb energy.

We have found that a promising Landau-based direction for modeling the N–SmZ_A–N_F system is the simple free energy shown in Eq. 1, proposed by Shiba and Ishibashi (48, 49), and applied to describe incommensurate AF in thiourea ($SC(NH_2)_2$) (50) and sodium nitrite ($NaNO_2$) (51, 52):

$$F_{IS} = \frac{A(T)}{2}P_z^2 + \frac{B}{4}P_z{}^4 + \frac{C}{6}P_z{}^6 - \alpha\left(\frac{\partial P_z}{\partial y}\right)^2 + \frac{\beta}{2}\left(\frac{\partial^2 P_z}{\partial y^2}\right)^2 + \frac{\eta}{2}P_z{}^2\left(\frac{\partial P_z}{\partial y}\right)^2 - P_z E_z, \quad [1]$$

Here ($\alpha > 0$, β,$\eta > 0$), ($B < 0$, $C > 0$), and the polarization inverse susceptibility is $\chi_P(T)^{-1} = A(T) = a(T - T_{oF})$. This free-energy functional can be obtained as a mean-field approximation to the ferroelectric Ising Hamiltonian with dipolar interactions, with the key feature that the—$\alpha(\partial P_z/\partial y)^2$ term is negative, which arises from the above mentioned F/AF frustration (53). F_{IS} has been used extensively in the analysis of soft matter modulation instabilities (36) and a variety of structural and dynamic experiments on modulated antiferroelectric phases (54–62).

Of particular relevance here is its successful application to the paraelectric–incommensurate modulated antiferroelectric–ferroelectric (P–A–F) phase sequences in $SC(NH_2)_2$ (63–65) and $NaNO_2$ (60, 61), as these exhibit key features similar to those of our observations of the binary N–N_F /N–SmZ_A–N_F phase behavior of Fig. 1, and of the SmZ_A phase. Applied to the RM734/DIO system, the dipolar Ising system and its F_{IS} mean field appear to contain the essential physics as described below, with the transition a phenomenon of fluctuations in P_z, acting under competition between isotropic local ferroelectric ordering, and conditions of strong anisotropy and frustration introduced by dipole–dipole interactions.

Although the F_{IS} model is limited to treating the 1D behavior of the single polarization component $P_z(y)$, there is good reason to believe that it can be usefully applied to the SmZ_A. The experiments show that the SmZ_A is lamellar and antiferroelectric, with layers of alternating polarization $\boldsymbol{P}(y)$, as sketched in Fig. 2*E*(1,2). Some flexoelectrically induced tilt (splay) modulation $\theta(y)$ must be present in such a modulated phase by symmetry [as drawn in Fig. 2*E*(1)], and the coupling of splay and $\boldsymbol{P}$ has been invoked as a potential driving force for the transition to a modulated state (5, 66–69) However, as also indicated in Fig. 2*E*(1), and not considered in previous theory in the ferroelectric nematic realm, splay of $\boldsymbol{P}(\boldsymbol{r})$ generates polarization charge

$\rho(\boldsymbol{r}) = -\nabla\cdot\boldsymbol{P}(\boldsymbol{r})$, making the gray stripes in Fig. 2*E*(1) negatively charged and the white stripes positively charged, which, in turn, generates a field (in red), which acts to reduce $\theta(y)$ and the splay deformation. The strength of this effect is parameterized by the length $\xi_P = \sqrt{(\varepsilon_{LC}K/P^2)}$, which in the characteristic distance from defects or surfaces within which splay deformation of $\boldsymbol{n}$ can remain

(69). At the lower temperatures in the SmZ_A range, with Frank elastic constant $K \sim 2$ pN, polarization within the SmZ_A layers $P > 3\ \mu C/cm^2$ (Fig. 5), and $\varepsilon_{LC} \sim 5$, we find $\xi_P < 0.3$ nm. The resulting condition, $\xi_P << w$, means that electrostatic interactions dominate the texture of the phase, overwhelming flexoelectricity and effectively forcing P_y to zero, as in Fig. 2*E*(2). The only charge-free variations in the resulting P_z are $\partial P_z/\partial x$ and $\partial P_z/\partial y$, the latter stabilized by the leading gradient term in the F_{IS}, which enables the modulated antiferroelectric SmZ_A phase as an ordered state of a paraelectric free energy well, as follows:

(i) *The RM734/DIO binary phase diagram vs. concentration*—Applied to the N–SmZ_A–N_F system, F_{IS} describes the first-order mean-field transition into the N_F phase as one from a paraelectric free energy minimum at $P_z = 0$ to a ferroelectric nematic minimum at finite P_z. This transition is controlled primarily by the $A(T,c) = a(c)[T - T_{oF}(c)]$, $B(c)$, $C(c)$ terms of F_{IS} which, because it is first-order, have $B(c) < 0$ and $C(c) > 0$, and T_{oF} is the temperature at which the paraelectric minimum of F_{IS} disappears. The transition to the N_F phase exhibits ideal mixing behavior (9), such that $T_{oF}(c)$ extrapolates linearly between the DIO and RM734 values, and the transition entropy $\Delta S = a(c)B(c)/C(c)$ and polarization in the N_F phase at $T = T_o$ $P_z(c) = \sqrt{-B(c)/C(c)}$ are nearly constant, indicating that *a*, *B*, and *C* change little across the phase diagram (9). The divergence of the small-signal dielectric constant approaching the N_F transition in the paraelectric minimum given by F_{IS} is $\Delta\varepsilon \approx \varepsilon_{\|} \propto \chi_P(T) \propto 1/a(T - T_{oF})$. Both RM734 and DIO exhibit this behavior, as seen in *SI Appendix*, Fig. S14. In RM734 this divergence takes place in the paraelectric N phase, while in DIO it occurs entirely within the SmZ_A phase, manifest in Fig. 5 as the decreasing V_{FA} required to induce the N_F as it is approached. The first-order transition to the N_F occurs where the paraelectric and ferroelectric minima of have the same energy, at $T_{ZF} = T_{oF} + B^2/4aC = T_{oF} + \sim 2$ °C.

(ii) *The N_F is a single unmodulated phase across the binary phase diagram*—This weak dependence of *A, B,* and *C* on *c* is consistent with N_F being the same phase across the RM734/DIO phase diagram (9). Our observations indicate this to be the case, showing the N_F being a homogeneous (unmodulated) fluid ferroelectric nematic having: a) a nematic director, $\boldsymbol{n}(\boldsymbol{r})$, which is locally free to reorient in any direction, subject only to the mutual, field-induced, and surface interactions (no underlying lattice as in solid-state ferroelectrics); b) polarization $\boldsymbol{P}(\boldsymbol{r})$, locally parallel to $\boldsymbol{n}(\boldsymbol{r})$, forming a coupled $\boldsymbol{n}(\boldsymbol{r})$-$\boldsymbol{P}(\boldsymbol{r})$ orientation variable. $\boldsymbol{P}(\boldsymbol{r})$ does not differ observably in direction from $\boldsymbol{n}(\boldsymbol{r})$ in the N_F phase, but is observed to vary spatially in magnitude, for example in pure polarization-reversal walls (7); c) Frank elastic behavior with the addition of polarization-generated space–charge interactions.

(iii) *Modulation*—The paraelectric $P_z = 0$ minimum of F_{IS} exhibits a transition from the N to the SmZ_A phase where the spatially modulated $P_z(y) = P_q \cos q_M y$ about $\langle P_z \rangle = 0$ appears, as in Fig. 2*E*(1,2). This modulation is driven by the energy-reducing $-\boldsymbol{\alpha}(\partial P_z/\partial y)^2$ term of F_{IS}, its negative sign arising from the anisotropy of the dipole–dipole interaction in *H*. The finite-P_z free energy minimum of F_{IS} describes the N_F ferroelectric, low-temperature state, which in principle could have the magnitude P_z spatially modulated about $\langle P_z \rangle \sim \sqrt{-B/C}$. However, with P_z minimized at $P_z \sim \sqrt{-B/C}$, F_{IS} predicts that neither ferroelectric or antiferroelectric modulation of $P_z(y)$ is possible in the N_F for parameters that give the other features of the phase diagram, i.e., F_{IS} predicts that the SmZ_A modulation will disappear in the N_F, as observed (60, 66). Additionally, director orientational modulation has been proposed to appear in the N_F phase, driven by the coupling between P_z and director splay (4, 5), such that where P_z is nonzero it induces preferred local splay, $|\nabla \cdot \boldsymbol{n}| = \partial n_y/\partial y \propto P_z$, which can stabilize polarization/splay modulated states. However, as in Fig. 2*E*(2), space charge expels splay and in the N_F minimum, where the positive coeffiecient $(\partial P_z/\partial y)^2$ term dominates, the uniform ferroelectric is the ground state.

(iv) *Role of long-range dipolar interaction (Polarization space charge self energy)*—Longitudinal polarization variations, $\partial P_z/\partial z$, are also strongly opposed by polarization space charge, leading, as previously pointed out (7), to the polarization correlation fluctuations in nematic RM734 that are extremely extended in the *z* direction, and become more so upon approaching the transition (*SI Appendix*, Fig. S12). This is an important feature of the paranematic pretransitional behavior of RM734, that provides evidence for a combination of short-range ferroelectric interactions and long-range (dipole–dipole) electrostatic interactions establishing the correlations. The observation of the SmZ_A provides further evidence for this view. Aharony, in the detailed renormalization group analysis of polar ordering systems with Ising/dipolar interactions undergoing a paraelectric/ferroelectric phase transition, derived the polarization pair correlation function $\langle P_z(0)P_z(\boldsymbol{r})\rangle$ of the paraelectric N phase and its static structure factor, $\chi_P(\boldsymbol{q}) = \langle P_z(\boldsymbol{q})P_z(\boldsymbol{q})^*\rangle$, shown in *SI Appendix*, Fig. S12 (70). This form was also obtained from a mean-field model (71). $\chi_P(\boldsymbol{q})$ is written in *SI Appendix*, Eq. S1 and plotted as a contour in *SI Appendix*, Fig. S12, showing that its principal feature is the energetic stretching of longitudinal fluctuations of $P_z(\boldsymbol{r})$ (those in which $\rho_P = \partial P_z/\partial z$ is nonzero), in order to expel polarization space-charge ρ_P. These effects are evident in the polarization fluctuations of paranematic RM734, as shown in *SI Appendix*, Fig. S12, which also points out the additional important Aharony findings that the resulting anisotropy also makes the transition mean-field-like, rather than fluctuation-dominated with 3D Ising universality, and that the growth of correlation in *y* is the principal soft mode of the transition (72–74). The corresponding Landau mean field free energy description of the transition can be derived from the Ising/dipolar Hamiltonian (55, 75), and applying it to the SmZ_A phase results in the F_{IS} model of Eq. 1: a) the SmZ_A is the extreme limit of polarization space-charge expulsion where the ordering of the $P_z(\boldsymbol{r})$ into stripe or layer arrays having both $\langle P_z(\boldsymbol{r})\rangle = 0$ and $\partial P_z/\partial z = 0$ induces the complete expulsion of longitudinal space charge from the paraelectric minimum state. The F_{IS} model, by treating $P_z(y)$ as a function only of *y*, is by construction an embodiment of this limit. b) The Aharony polarization correlation function and the corresponding negative gradient term, $-\boldsymbol{\alpha}(\partial P_z/\partial y)^2$, in the Landau free energies like F_{IS}, express the frustration arising from the tendencies for head-to-tail (side-by-side) dipoles to be parallel (antiparallel), and make possible the periodic modulation of $P_z(y)$. This is predominately a P_z effect. A useful generalization of F_{IS} would be explicit treatment of the z dependence of $\boldsymbol{P}$.

(v) *The SmZ_A is an ordered antiferroelectric state of the paraelectric minimum*—Experimentally, the linearity vs. *c* of the N_F upper phase boundary, and its transition entropy that is weakly varying across the phase diagram and large compared with that of the N–SmZ_A transition, suggests that the N and SmZ_A phases are both features of the paraelectric minimum and that the N–SmZ_A phase change is a transition within the paraelectric minimum. This is the F_{IS} prediction: a paraelectric phase with a susceptibility for polarization diverging at the transition to the N_F in which the typical pretransition scenario approaching the transition to a ferroelectric phase is interrupted by an instability to an ordered (modulated antiferroelectric) state, in our case the SmZ_A. This instability occurs because of the decreasing energy cost of finite P_z as the transition to the N_F is approached.

The free energy of Eq.1 thus gives either an N–(T_{NF})–N_F or an N–(T_{NZ})–SmZ_A–(T_{ZF})–N_F phase sequence, depending on parameters, where the transition to the N_F phase is first-order, and the N – SmZ_A second-order or weakly first-order, as confirmed experimentally by the optical observations in Fig. 3*F* and by DSC (6) in DIO. An important feature of the N–SmZ_A transition is the temperature independence of q_M, having a value $q_M \sim 0.07 Å^{-1}$ even as a small pretransitional scattering bump in the N phase, and as scattering from a few remnant domains (Fig. 2*H* and *SI Appendix*, Figs. S4 and S5). In the F_{IS} energy, the antiferroelectric incommensurate (SmZ_A) phase is produced by frustration between the term forcing slope ($\alpha < 0$) and that resisting curvature ($\beta > 0$) of $P_z(y)$, producing a nearly temperature-independent modulation wavevector $\boldsymbol{q}_M$. Upon cooling, near $T \sim T_{NZ}$ the initially weak modulation of $P_z(y)$ is sinusoidal with wavevector $q_M \approx \sqrt{-\alpha/2\beta}$, determined mainly by α and β, and independent of the magnitude of P_z. Eq.1 correctly predicts the temperature dependence of $\boldsymbol{q}_M$, which comprises the 5% decrease in $\boldsymbol{q}_M$ with T through the SmZ_A range (Fig. 2*H*) contributed by the higher order η term. Specifically worth noting is the lack of a $q_M \propto \sqrt{T_{NZ} - T}$ anomaly at high temperatures in the SmZ_A, a feature of Landau models in which q_M is controlled directly by the coefficient of the P^2 term (4, 5, 76).

The weak variation in $\boldsymbol{q}_M(T)$ over the entire SmZ_A range in Fig. 2*H* is rather remarkable, given a) the decrease with T of the antiferroelectric–ferroelectric transition threshold field $E_{FA}(T)$ (Fig. 5*B*); b) the increase in the induced polarization P_{FA} (Fig. 5*B*); and (iii) the strong variation in scattering intensity (Fig. 2*G*), which combined indicate a significant change in layer structure over the same range. The SAXS scans exhibit only the fundamental peak of the scattering electron density modulation, which would generally be interpreted in smectics to indicate a sinusoidal electron density modulation. However, although the peak intensity $I_p(T)$ decreases for both large and small T (Fig. 2*G*), the layer structures must be very different near the two limits, in a way not describable by simply varying a sine-wave amplitude. If higher sinusoidal harmonics of $P_z(y)$ are included in the F_{IS} model, then $P_z(y)$ evolves on cooling from sinusoidal to approaching a solitonic or square waveform for $T \sim T_{ZF}$, in which alternating +/– plateaus of maximum $|P_z(y)|$ and high electron-density [based on the higher mass density of the N_F relative to the N (77) are separated by narrow solitonic domain walls of width $d(T)$ where the sign of $P_z(y)$ changes and electron density is lower (56–59). The decrease in the non-resonant SAXS peak intensity as T approaches T_{ZF} in Fig. 2*G* will depend on $d(T)$ approximately as $I_p(T) \propto I_{pmax} \sin^2(\pi\, d(T)/w_M)$. The question of the constancy of $q_M(T)$ has also been considered by Kats, who perceptively speculated that the M2 phase could be a modulated antiferroelectric (78) and suggested that the N to M2 transition would then be a "weak-crystallization" phenomenon, with $q_M(T)$ constrained as in weak-crystallization theory (79).

(vi) *The temperature*–electric field (T, E_z) phase diagram—Fig. 5*A* shows that the transition to the N_F phase can be induced by an electric field applied along the director, with $E_z(T)_{ZF}$, the field required to induce the transition, shown as a function of temperature in Fig. 5*B*. A similar field-induced shift in the transition to the ferroelectric phase has been observed in thiourea and sodium nitrite, and is a prominent feature of the P–A–F experimental phase diagrams obtained by Shiba and Ishibashi and the theoretical fits calculated from Eq.1 (60, 61) and shown in *SI Appendix*, Fig. S13. The (*T, E*) thiourea phase diagram (61), obtained using Eq.1 with $B > 0$ and $C = 0$, matches the optical (4) and neutron scattering (66) data for thiourea, and describes well the DIO (T, E_z) phase behavior with appropriate temperature and field scaling. A remarkable feature of both the IC data in $NaNO_2$ and the predictions of Eq.1 is that in the entire IC area of the (*T, E*) phase diagram, the modulation wavevector is nearly constant at $q_M = \sqrt{-\alpha/2\beta}$, changing by only 20% over the entire (T, E_z) range (60, 61). Application of the F_{IS} model to the SmZ_A case would therefore suggest that in the N_F – SmZ_A phase coexistence condition obtained upon reducing the field in Fig. 5, the SmZ_A domains have a nearly field-independent periodicity $q_M \sim 2\pi/(9$ nm). This has not yet been tested experimentally.

(vii) *Concentration dependence of the SmZ_A phase*—α (c) and β (c) also determine the temperature range of the SmZ_A according to $T_{NZ} - T_{ZF} = \alpha^2/2a\,\beta$, (60, 61) suggesting that α (c) changes sign at the SmZ_A endpoint at $c \sim 40\%$, and that measurement of $q_M(c) = \sqrt{-\alpha(c)/2\beta(c)}$ will be a key experiment for determining the dependence of these parameters on c. In any case, given that non-zero $\partial P_z/\partial y$ is favored in DIO, it may be that $\partial P_z/\partial y$ will generally at least not be strongly suppressed in the paranematic phase of ferroelectric nematic materials. Such a tendency is already evident in RM734, in the dominance of $\partial P_z/\partial y$ fluctuations in its paranematic phase (*SI Appendix*, Fig. S12).

Data, Materials, and Software Availability. Data and videos data have been deposited in an Open Science Framework repository named "Smectic ZA". The link is https://osf.io/9fev2/ and the DOI is DOI: 10.17065/OSF.IO/9fev2/. (80)

ACKNOWLEDGMENTS. This work was supported by NSF Condensed Matter Physics Grants Division of Materials Research (DMR) 1710711 and DMR 2005170, and by Materials Research Science and Engineering Center Grant DMR 1420736. This research used the microfocus Soft Matter Interfaces beamline 12-ID of the National Synchrotron Light Source II, a U.S. Department of Energy (DOE) Office of Science User Facility operated for the DOE Office of Science by Brookhaven National Laboratory under Contract No. DE-SC0012704. We also acknowledge the use of beam line 11.0.1.2 of the Advanced Light Source at the Lawrence Berkeley National Laboratory supported by the Director of the Office of Science, Office of Basic Energy Sciences, of the U.S. DOE under Contract No. DE-AC02-05CH11231. Substantial portions of this work overlap with the PhD dissertation of X.C. ("New Phases and Phenomena of the Ferroelectric Nematic Realm," University of Colorado, 2022).

Author affiliations: [a]Department of Physics and Soft Materials Research Center, University of Colorado, Boulder, CO 80309; [b]Department of Chemistry and Soft Materials Research Center, University of Colorado, Boulder, CO 80309; [c]Brookhaven National Laboratory, National Synchrotron Light Source-II, Upton, NY 11973; and [d]Advanced Light Source, Lawrence Berkeley National Laboratory, Berkeley, CA 94720

1. P. Debye, Einige Resultate einer kinetischen Theorie der Isolatoren. *Physikalische Zeitschrift* **13**, 97–100 (1912).
2. M. Born, Über Anisotrope Flüssigkeiten. Versuch Einer Theorie Der Flüssigen Kristalle Und Des Elektrischen Kerr-Effekts In Flüssigkeiten. *Sitzungsber. Preuss. Akad Wiss.* **30**, 614–650 (1916).
3. R. J. Mandle, S. J. Cowling, J. W. Goodby, A nematic to nematic transformation exhibited by a rod-like liquid crystal. *Phys. Chem. Chem. Phys.* **19**, 11429–11435 (2017), 10.1039/C7CP00456G.
4. A. Mertelj *et al.*, Splay nematic phase. *Phys. Rev. X* **8**, 041025 (2018), 10.1103/PhysRevX.8.041025.
5. N. Sebastian *et al.*, Ferroelectric-ferroelastic phase transition in a nematic liquid crystal. *Phys. Rev. Lett.* **124**, 037801 (2020), 10.1103/PhysRevLett.124.037801.
6. H. Nishikawa *et al.*, A fluid liquid-crystal material with highly polar order. *Adv. Mater.* **29**, 1702354 (2017), 10.1002/adma.201702354.
7. X. Chen *et al.*, First-principles experimental demonstration of ferroelectricity in a thermotropic nematic liquid crystal: Spontaneous polar domains and striking electro-optics. *Proc. Natl. Acad. Sci. U. S. A.* **117**, 14021–14031 (2020), 10.1073/pnas.2002290117.
8. J. Li *et al.*, Development of ferroelectric nematic fluids with giant-ε dielectricity and nonlinear optical properties. *Sci. Adv.* **7**, eabf5047 (2021), 10.1126/sciadv.abf5047.
9. X. Chen *et al.*, Ideal mixing of paraelectric and ferroelectric nematic phases in liquid crystals of distinct molecular species. *Liq. Cryst.* **49**, 1531–1544 (2022).
10. R. J. Mandle, S. J. Cowling, J. W. Goodby Structural variants of RM734 in the design of splay nematic materials, *Liq. Cryst.* **48**, 1780-1790 (2021), 10.1080/02678292.2021.1934740.
11. G. Friedel, Les états mésomorphes de la matière. *Ann. Phys. (Paris)* **18**, 273–474 (1922), 10.1051/anphys/192209180273.

12. G. Friedel, F. Grandjean, Cristaux liquides. Réponse à MM. G. Friedel, et F. Grandjean a M. O. Lehmann. *Bull. de Minéral.* **33**, 300–317 (1910), 10.3406/bulmi.1910.3440.
13. H. Sackmann, D. Demus, The polymorphism of liquid crystals. *Mol. Cryst. Liq. Cryst.* **2**, 81–102 (1966), 10.1080/15421406608083062.
14. N. A. Clark, Antiferroelectric Smectic Ordering as a Prelude to the Ferroelectric Nematic: Introducing the Smectic Z Phase. in *Plenary Lecture 2, 18th International Conference on Ferroelectric Liquid Crystals*, (FLC2021, Ljubljana, Slovenia, 2021).
15. H. Nishikawa *et al.*, Nano-clustering mediates phase transitions in a diastereomerically-stabilized ferroelectric nematic system. *Commun. Mater.* **3**, 89 (2022), 10.1038/s43246-022-00312-9.
16. C. R. Safinya *et al.*, High-resolution x-ray study of a smectic-A – smectic-C phase transition. *Phys. Rev. B* **21**, 4149–4153 (1980), 10.1103/PhysRevB.21.4149o.
17. T. P. Rieker *et al.*, Chevron' local layer structure in surface-stabilized ferroelectric smectic-C cells. *Phys. Rev. Lett.* **59**, 2658–2661 (1987), 10.1103/PhysRevLett.59.2658.
18. N. A. Clark, T. P. Rieker, Smectic C "chevron", a planar liquid-crystal defect: Implications for the surface-stabilized ferroelectric liquid-crystal geometry. *Phys. Rev. A. Rapid Commun.* **37**, 1053–1056 (1988), 10.1103/physreva.37.1053.
19. N. A. Clark, T. P. Rieker, J. E. Maclennan, Director and layer structure of SSFLC cells. *Ferroelectrics* **85**, 79–97 (1988), 10.1080/00150198808007647.
20. T. P. Rieker, N. A. Clark, G. S. Smith, C. R. Safinya, Layer and director structure in surface stabilized ferroelectric liquid crystal cells with non-planar boundary conditions. *Liq. Cryst.* **6**, 565–576 (1989), 10.1080/02678298908034176.
21. T. P. Rieker, N. A. Clark, C. R. Safinya, Chevron layer structures in surface stabilized ferroelectric liquid crystal (SSFLC) cells filled with a material which exhibits the chiral nematic to smectic C* phase transition. *Ferroelectrics* **113**, 245–256 (1991), 10.1080/00150199108014067.
22. S. T. Lagerwall, *Ferroelectric and Antiferroelectric Liquid Crystals* (Wiley VCH, Weinheim, ISBN 3-527-2983 1-2, 1999).
23. Y. Takanishi, Y. Ouchi, H. Takezoe, Chevron layer structure in the smectic-A phase of 8CB. *Jpn. J. Appl. Phys. Part 2-Lett.* **28**, L487–L489 (1989), 10.1143/JJAP.28.L487.
24. X. Cheng *et al.*, Calamitic bolaamphiphiles with (semi)perfluorinated lateral chains: Polyphilic block molecules with new liquid crystalline phase structures. *J. Am. Chem. Soc.* **125**, 10977–10996 (2003), 10.1021/ja036213g.
25. J. O. Rädler, I. Koltover, T. Salditt, C. R. Safinya, Structure of DNA-cationic liposome complexes: dna intercalation in multilamellar membranes in distinct interhelical packing regimes. *Science* **275**, 810–814 (1997), 10.1126/science.275.5301.810.
26. R. A. Reddy, C. Tschierske, Bent-core liquid crystals: Polar order, superstructural chirality and spontaneous desymmetrisation in soft matter systems. *J. Mater. Chem.* **16**, 907 (2006), 10.1039/B504400F.
27. J. V. Selinger, Director deformations, geometric frustration, and modulated phases in liquid crystals. *Annual Review of Condensed Matter Physics* **13**, 49-71 (2022) 10.1146/annurev-conmatphys-031620-105712.
28. X. Chen *et al.*, Polar in-plane surface orientation of a ferroelectric nematic liquid crystal: Polar monodomains and twisted state electro-optics. *Proc. Natl. Acad. Sci. U.S.A.* **118**, e2104092118 (2021), 10.1073/pnas.2104092118.
29. P. G. de Gennes, An analogy between superconductors and smectics A. *Solid State Commun.* **10**, 753–756 (1972), 10.1016/0038-1098(93)90291-T.
30. H. Birecki, R. Schaetzing, F. Rondelez, J. D., Litster light-scattering study of a smectic-A phase near the smectic-A – nematic transition. *Phys. Rev. Lett.* **36**, 1376–1379 (1976), 10.1103/PhysRevLett.36.1376.
31. S. Brown *et al.*, Multiple polar and non-polar nematic phases. *Chemphyschem* **22** 2506–2510 (2021), 10.1002/cphc.202100644.
32. P. Nacke, A. Manabe, M. Klasen-Memmer, M. Bremer, F. Giesselmann, "New example of a ferroelectric nematic phase material" in Poster P2 in *18th International Conference on Ferroelectric Liquid Crystals (FLC2021)* Ljubljana, Slovenia, (2021) Institute Josef Stefan, Ljubliana.
33. M. Seul, D. Andelman, Domain shapes and patterns: The phenomenology of modulated phases. *Science* **267**, 476–483 (1995), 10.1126/science.267.5197.476.
34. M. Marder, H. L. Frisch, J. S. Langer, H. M. McConnell, Theory of the intermediate rippled phase of phospholipid bilayers. *Proc. Natl. Acad. Sci. U.S.A.* **81**, 6559–6561 (1984), 10.1073/pnas.81.20.6559.
35. A. E. Jacobs, G. Goldner, D. Mukamel, Modulated structures in tilted chiral smectic films. *Phys. Rev. A.* **45**, 5783–5788 (1992), 10.1103/PhysRevA.45.5783.
36. G. A. Hinshaw Jr., R. G. Petschek, Transitions and modulated phases in centrosymmetric ferroelectrics: Mean-field and renormalization-group predictions. *Phys. Rev. B.* **37**, 2133–2155 (1988), 10.1103/PhysRevB.37.2133.
37. J. W. Felix, D. Mukamel, R. M. Hornreich, Novel class of continuous phase transitions to incommensurate structures. *Phys. Rev. Lett.* **57**, 2180–2183 (1986), 10.1103/PhysRevLett.57.2180.
38. K. De'Bell, A.B. MacIsaac, J.P. Whitehead, Dipolar effects in magnetic thin films and quasi-two-dimensional systems. *Rev. Mod. Phys.* **72**, 225–257 (2000), 10.1103/RevModPhys.72.225.
39. G. Szabo, G. Kadar, Magnetic hysteresis in an ising-like dipole-dipole model. *Phys. Rev. B.* **58**, 5584–5587 (1998), 10.1103/PhysRevB.58.5584.
40. H. Z. Cummins, Experimental studies of structurally incommensurate crystal phases. *Phys. Rep.* **185**, 211–409 (1980), 10.1016/0370-1573(90)90058-A.
41. R. Blinc, A. P. Levanyuk, *Incommensurate Phases in Dielectrics: Volume 1 Fundamentals; Volume 2 Materials* (Elsevier Science Publishers, Amsterdam, 1986).
42. A. B. MacIsaac, J. P. Whitehead, M. C. Robinson, K. De'Bell, Striped phases in two-dimensional dipolar ferromagnets. *Phys. Rev. B.* **51**, 16033–16045 (1995), 10.1103/PhysRevB.51.16033.
43. M. Grousson, G. Tarjus, P. Viot, Phase diagram of an Ising model with long-range frustrating interactions: A theoretical analysis. *Phys. Rev. E.* **62**, 7781–7792 (2000), 10.1103/physreve.62.7781.
44. M. Grousson, G. Tarjus, P. Viot, Monte Carlo study of the three-dimensional Coulomb frustrated Ising ferromagnet. *Phys. Rev. E.* **64**, 036109 (2000), 10.1103/PhysRevE.64.036109.
45. R. M. Hornreich, M. Luban, S. Shtrikman, Critical behavior at the onset of k-Space instability on the l line. *Phys. Rev. Lett.* **35**, 1678–1681 (1975), 10.1103/PhysRevLett.35.1678.
46. S. A. Pighín, S. A. Cannas, Phase diagram of an Ising model for ultrathin magnetic films: Comparing mean field and Monte Carlo predictions. *Phys. Rev. E.* **75**, 224433 (2007), 10.1103/PhysRevB.75.224433.
47. M. Y. Choi, Domain-wall pinning in the incommensurate phase of sodium nitrite. *Phys. Rev. B.* **37**, 5874–5876 (1988), 10.1103/PhysRevB.37.5874.
48. Y. Ishibashi, H. Shiba, Successive phase-transitions in ferroelectric NaNO2 and SC(NH2)2. *J. Phys. Soc. Japan* **45,** 409–413 (1978), 10.1143/JPSJ.45.409.
49. Y. Ishibashi, H. Shiba, Incommensurate-commensurate phase-transitions in ferroelectric substances. *J. Phys. Soc. Japan* **45**, 1592–1599 (1978), 10.1143/JPSJ.44.159.
50. Y. Shiozaki, Satellite x-ray scattering and structural modulation of thiourea. *Ferroelectrics* **2**, 245–260 (1978), 10.1080/00150197108234099.
51. S. Tanisaki, I. Shibuya, Microdomain structure in paraelectric phase of NaNO2. *J. Phys. Soc. Japan* **16**, 579 (1961), 10.1143/JPSJ.16.579.
52. Y. Yamada, S. Hoshino, I. Shibuya, Phase transition in NaNO2. *J. Phys. Soc. Japan* **18**, 1594–1603 (1963), 10.1143/JPSJ.18.1594.
53. M. Y. Choi, Domain-wall pinning in the incommensurate phase of sodium nitrite. *Phys. Rev. B* **37**, 5874–5876 (1988), 10.1103/PhysRevB.37.5874.
54. M. Iwata, H. Orihara, Y. Ishibashi, Phenomenological theory of the linear and nonlinear dielectric susceptibilities in the type-II incommensurate phase. *J. Phys. Soc. Japan* **67**, 3130–3136 (1998), 10.1143/jpsj.67.3130.
55. S. V. Berezovsky, Soliton regime in the model with no Lifshitz invariant. arXiv:cond-mat/9909079 (1999) Accessed 6 July 2022.
56. I. Aramburu, G. Madariaga, J. M. Perez-Mato, Phenomenological model for type-II incommensurate phases having a soliton regime: Thiourea case. *Phys. Rev. B.* **49**, 802–814 (1994), 10.1103/PhysRevB.49.802.
57. I. Aramburu, G. Madariaga, J. M. Perez-Mato, A structural viewpoint on the sine-Gordon equation in incommensurate phases. *J. Phys. Condens. Matter* **7**, 6187–6196 (1995), 10.1088/0953-8984/7/31/003.
58. D. Durand, F. Denoyer, D. Lefur, Neutron diffraction study of sodium nitrite in an applied electric field. *J. de Phys.* **44**, L207–L216 (1983), 10.1051/jphyslet:01983004405020700.
59. D. Durand, F. Denoyer, R. Currat, M. Lambert, "Chapter 13 - Incommensurate phase in NaNO2" in *Incommensurate Phases in Dielectrics: 2 Materials*, R. Blinc, A. P. Levanyuk, Eds. (Elsevier Science Publishers, Amsterdam, 1986), 10.1016/B978-0-444-86970-8.50010-X.
60. G. H. F. van Raaij, K. J. H. van Bemmel, T. Janssen, Lattice models and Landau theory for type-II incommensurate crystals. *Phys. Rev. B.* **62**, 3751–3765 (2000), 10.1103/PhysRevB.62.3751.
61. A. E. Jacobs, C. Grein, F. Marsiglio, Rippled commensurate state: A possible new type of incommensurate state. *Phys. Rev. B.* **29**, 4179–4181 (1984), 10.1103/PhysRevB.29.4179.
62. A. E. Jacobs, Intrinsic domain-wall pinning and spatial chaos in continuum models of one-dimensionally incommensurate systems. *Phys. Rev. B.* **33**, 6340–6345 (1986), 10.1103/PhysRevB.33.6340.
63. P. Lederer, C. M. Chaves, Phase diagram of thiourea at atmospheric pressure under electric field: A theoretical analysis. *J. de Phys. Lett.* **42**, L127–L130 (1981), 10.1051/jphyslet:01981004206012700.
64. J. P. Jamet, Electric field phase diagram of thiourea determined by optical birefringence. *J. Phys. Lett.* **1981**, L123–L12 (1981), 10.1051/jphyslet:01981004206012300.
65. F. Denoyer, R. Currat, *Chapter 14 - Currat, Modulated Phases in Thiourea - Incommensurate phases in dielectrics: 2 Materials*, R. Blinc, A.P. Levanyuk, Ed. (Elsevier Science Publishers, Amsterdam, 1986), 10.1016/B978-0-444-86970-8.50010-X.
66. M. P. Rosseto, J. V. Selinger, Theory of the splay nematic phase: Single versus double splay, *Phys. Rev. E.* **101**, 052707 (2020).
67. M. Copic, A. Mertelj, Q-tensor model of twist-bend and splay nematic phases. *Phys. Rev. E.* **101**, 022704 (2020), 10.1103/PhysRevE.101.022704.
68. N. Sebastian, M. Copic, A. Mertelj, Ferroelectric nematic liquid crystalline phases. *Phys. Rev. E.* **106**, 021001 (2022), 10.1103/PhysRevE.106.021001.
69. Z. Zhuang, J. E. Maclennan, N. A. Clark, Device applications of ferroelectric liquid crystals: Importance of polarization charge interactions. *Proc. Soc. Photo-Optical Instrum. Eng.* **1080**, 110–114 (1989), 10.1117/12.976407.
70. A. Aharony, Critical behavior of magnets with dipolar interactions. V. Uniaxial magnets in *d*-dimensions. *Phys. Rev. B* **8**, 3363–3370 (1973), 10.1103/PhysRevB.8.3363.
71. A. I. Larkin, D. E. Khmel'nitskii, Phase transition in uniaxial ferroelectrics. *Soviet Phys. JETP* **29**, 1123–1128 (1969).
72. J. Kotzler, Critical phenomena in dipolar magnets. *J. Magn. Magn. Mater.* **54–57**, 649–654 (1986), 10.1016/0304-8853(86)90197-6.
73. J. Als-Nielsen, Experimental test of renormalization group theory on the uniaxial, dipolar coupled ferromagnet LiTbF4. *Phys. Rev. Lett.* **37**, 1161–1164 (1976), 10.1103/PhysRevLett.37.1161.
74. J. Als-Nielsen, R. J. Birgeneau, Mean field theory, the Ginzburg criterion, and marginal dimensionality of phase transitions. *Am. J. Phys.* **45**, 554–560 (1977), 10.1119/1.11019.
75. S. M. Belim, Critical behavior of isotropic three dimensional systems with dipole-dipole interactions. *J. Exp. Theoret. Phys.* **116**, 963–974 (2013), 10.1134/S1063776113050178.
76. M. P. Rosseto, J. V. Selinger, Theory of the splay nematic phase: Single versus double splay nematic phase. *Phys. Rev. E.* **101**, 052707 (2020).
77. R. J. Mandle, N. Sebastián, J. Martinez-Perdiguero, A. Mertelj, On the molecular origins of the ferroelectric splay nematic phase. *Nat. Commun.* **12**, 4962 (2021), 10.1038/s41467-021-25231-0.
78. E. I. Kats, Stability of the uniform ferroelectric nematic phase. *Phys. Rev. E.* **103**, 012704 (2021), 10.1103/PhysReE.103.012704.
79. E. I. Kats, V. V. Lebedev, A. R. Muratov, Weak crystallization theory. *Phys. Rep.* **228**, 1–91 (1993), 10.1016/0370-1573(93)90119-X.
80. M. A. Glaser, J. E. MacLennan, X. Chen, Smectic ZA. *Open Science Framework (OSF)* https://osf.io/PFTGR/. Deposited 11 June 2022.